

Banner appropriate to article type will appear here in typeset article

# Anomalous Reynolds stress and dynamic mechanisms in two-dimensional elasto-inertial turbulence of viscoelastic channel flow

Haotian Cheng<sup>1</sup>, Hongna Zhang<sup>1</sup>†, Wenhua Zhang<sup>1</sup>‡, Suming Wang<sup>1</sup>, Xiaobin Li<sup>1</sup>, Yuke Li<sup>2</sup> and Fengchen Li<sup>1</sup>

<sup>1</sup>State Key Laboratory of Engine, Tianjin University, Tianjin 300350, PR China

<sup>2</sup>College of Shipbuilding Engineering, Harbin Engineering University, Harbin 150001, PR China and National Key Laboratory of Ship Structural Safety, Harbin 150001, Heilongjiang, PR China

(Received xx; revised xx; accepted xx)

Elasto-inertial turbulence (EIT) has been demonstrated to be able to sustain in two-dimensional (2D) channel flow; however the systematic investigations on 2D EIT remain scarce. This study addresses this gap by examining the statistical characteristics and dynamic mechanisms of 2D EIT, while exploring its similarities to and differences from three-dimensional (3D) EIT. We demonstrate that the influence of elasticity on the statistical properties of 2D EIT follows distinct trends compared to those observed in 3D EIT and drag-reducing turbulence (DRT). These differences can be attributed to variations in the underlying dynamical processes. As nonlinear elasticity increases, the dominant dynamic evolution in 3D flows involves the gradual suppression of inertial turbulence (IT). In contrast, 2D flows exhibit a progressive enhancement of EIT. More strikingly, we identify an anomalous Reynolds stress in 2D EIT that contributes negatively to flow resistance, a behavior opposite to that of IT. Quadrant analysis of velocity fluctuations reveals the predominance of motions in the first and third quadrants. These motions are closely associated with polymer sheet-like extension structures, which are inclined from the near-wall region toward the channel center along the streamwise direction. Finally, we present the dynamical budget of 2D EIT, which shows significant similarities to that of 3D EIT, thereby providing compelling evidence for the objective existence of the 2D nature of EIT.

**Key words:** viscoelasticity, turbulence simulation, turbulence theory

## 1. Introduction

Viscoelastic fluids are ubiquitous in industrial production and biological fluids and exhibit distinctive flow behaviors, especially turbulence drag reduction (TDR) at high Reynolds number (Re, Toms (1949)) and the elastic turbulence (ET) at extremely low Re (Grossman

† Email address for correspondence: hongna@tju.edu.cn

‡ Email address for correspondence: zhangwh2022@tju.edu.cn

**Abstract must not spill onto p.2**

(2001)). The early turbulence (Ostwald & Auerbach (1926)) and the maximum drag reduction (MDR) asymptote of TDR (Virk et al. (1970)) in viscoelastic fluid have long been mysteries. The discovery of elasto-inertial turbulence (EIT) by Samanta et al. (2013) and Dubief et al. (2013) provides a harmonizing explanation for both the early turbulence and the MDR phenomena, opening up a new avenue for viscoelastic turbulence.

Unlike elastic turbulence (ET) at extremely low  $Re$  and inertial turbulence (IT), elasto-inertial turbulence (EIT) is primarily governed by elastic nonlinearity with non-negligible inertial nonlinearity. Consequently, the structure and self-sustaining mechanisms of EIT are closely linked to elastic instability (Dubief et al. (2023)). The friction factor of EIT follows the MDR asymptote and exhibits characteristics consistent with the MDR state, such as a mean velocity profile approaching the Virk asymptote and negligible Reynolds stress (Warholic et al. (1999); Min et al. (2003)). Recent studies have revealed that the flow topology of EIT differs significantly from that of IT. While IT is typically characterized by small-scale hairpin vortex structures, EIT is marked by localized, strongly elongated sheet-like structures formed by polymer extension in the streamwise direction, accompanied by alternating spanwise cylindrical structures (Dubief et al. (2013, 2023); Terrapon et al. (2015)). The formation of these unique structures is attributed to the energy transfer mechanism from polymer stress work fluctuations to turbulent kinetic energy (Dubief et al. (2013)) and the role of polymeric pressure fluctuations (Terrapon et al. (2015)). Additionally, experimental studies have identified the characteristic chevron-shaped streak structures of EIT, which transition into inclined near-wall streaks and shear layers as inertia increases (Choueiri et al. (2021)). Regarding the self-sustaining mechanism of EIT, we conducted systematic analyses by incorporating EIT-related dynamics into drag-reducing turbulence (DRT) (Zhang et al. (2022)). This approach allowed us to redefine the self-sustaining cycle of DRT, where IT-related and EIT-related dynamics coexist. Our findings reveal that IT-related dynamics is gradually supplanted by EIT-related dynamics in DRT as elasticity increases (Zhang et al. (2022)). Despite these advancements, the unique dynamic mechanisms underlying EIT remain an active area of research (Dubief et al. (2023)).

The delayed recognition of elasto-inertial turbulence (EIT) stems partly from its overlap with inertial turbulence (IT) across a broad parameter space (Dubief et al. (2023)). Historically, the maximum drag reduction (MDR) state was interpreted through the lens of polymer-modulated IT, leading some studies (Xi et al. (2010a,b, 2016); Graham (2014); Wang et al. (2017)) to classify it as a marginal IT state. Recent advancements have shifted focus toward EIT-dominated flows as the prevailing paradigm. A compelling experimental observation—complete relaminarization of IT within specific polymer concentration ranges at fixed  $Re$  (Choueiri et al. (2018))—validates the distinct existence of EIT and confirms that the MDR state in viscoelastic drag-reducing turbulence (DRT) fundamentally represents EIT. This relaminarization phenomenon has been corroborated numerically (Zhang et al. (2022)). However, our recent findings reveal that the MDR state’s nature is intrinsically tied to the polymer’s maximum extension length  $L^2$ : while the MDR state of FENE-P fluids with small  $L^2$  corresponds to marginal IT, it transitions to EIT-dominated behavior at larger  $L^2$  values (Wang et al. (2023)). Notably, Sid et al. (2018) identified 2D elasto-inertial instability and obtained the sustained EIT in 2D direct numerical simulations (DNS), mirroring the existence of elastic turbulence (ET) in 2D periodic Kolmogorov flow (Berti et al. (2008)). Recent experimental work (Warwaruk et al. (2024)) further demonstrates that viscoelastic flows exhibit more pronounced 2D straining motions compared to conventional IT, strongly supporting the hypothesis of an inherently 2D nature in EIT. While EIT in 3D DNS and real-world flows necessarily manifests in three dimensions, its interplay with IT complicates targeted investigations. Crucially, 2D DNS offers a unique advantage by effectively isolating

IT, thereby enabling dedicated studies of EIT while substantially reducing computational demands.

Subsequently, the study of elastoinertial turbulence (EIT) has experienced rapid expansion through 2D DNS, owing to their relatively low grid requirements and computational efficiency. This computational accessibility has enabled comprehensive investigations into EIT's fundamental characteristics, intrinsic nature, transitional mechanisms, and underlying origins. Notable contributions include the work of Gillissen (2019), who performed 2D DNS of viscoelastic fluid flows across varying polymer concentrations, establishing a classification system distinguishing strongly and weakly coupled EIT regimes based on structural features. A critical divergence between 2D and 3D flow dynamics was revealed by Zhu et al. (2021), demonstrating that unlike three-dimensional flows where friction factors converge to the MDR asymptote with increasing Weissenberg number ( $Wi$ ), their 2D counterparts exhibit no such convergent behavior. The field advanced significantly with the identification of dual instability mechanisms governing EIT inception: wall-mode instability mediated by Tollmien-Schlichting waves (Shekar et al. (2019, 2020, 2021)) and center-mode instability driven by nonlinear elastoinertial traveling waves (Page et al. (2020); Choueiri et al. (2021)). These distinct modes are spatially differentiated, with wall-mode disturbances concentrating near boundary surfaces and center-mode perturbations localizing around flow domain midlines (Chaudhary et al. (2019)). Contemporary research consensus, however, increasingly supports wall-mode dominance in EIT generation, as evidenced by recent studies (Zhang et al. (2024); Beneitez et al. (2024a); Shekar et al. (2021)). This perspective gains further validation from the discovery of polymer diffusive instability (PDI), which has been classified as a wall-mode phenomenon (Couchman et al. (2024); Beneitez et al. (2024b)). Our numerical visualization studies provide direct evidence of wall-mode-induced EIT dynamics, revealing that the cyclical fracture and regeneration of polymer sheet-like structures constitutes the fundamental self-sustenance mechanism (Zhang et al. (2024)). Crucially, we have identified the minimal flow unit (MFU) necessary for EIT initiation and maintenance by 2D DNS, establishing a critical foundation for developing numerical criteria for EIT identification. This work further quantifies the  $Wi$ -dependent scaling of MFU dimensions while elucidating the underlying physical rationale.

The structural parallels between two- and three-dimensional flows, coupled with the absence of conventional Newtonian near-wall structures, led Sid et al. (2018) to propose that EIT becomes the dominant regime in MDR state at elevated  $Wi$ . This interpretation implies that the 3D MDR state represents a hybrid regime rather than pure EIT. Fundamental differences emerge between 2D and 3D flows due to the coexistence of inertial turbulence (IT) in three-dimensional configurations, manifesting in divergent flow dynamics and parameter response characteristics. Recent comparative studies by Zhu et al. (2021) revealed contrasting  $Wi$ -dependent trends in friction factor evolution: while 3D flows exhibit asymptotic convergence toward MDR levels, their 2D counterparts demonstrate non-convergent behavior. Notably, this 3D convergence does not imply stabilization into pure 2D EIT dynamics, as underlying flow structures continue evolving even at high  $Wi$ . This conceptual framework positions the 3D MDR state not as a pure EIT analog, but rather as a composite regime incorporating multiple dynamical patterns sustained through elastic effects. Zhu et al. (2021) further identified three distinct dynamical cycles within the MDR state, with 2D EIT representing just one phase in this spectrum. Despite significant advances in 2D EIT characterization (Sid et al. (2018); Shekar et al. (2021); Zhu et al. (2021); Dubief et al. (2022)), critical gaps persist in systematic quantification of its statistical signatures and underlying dynamical mechanisms.

To address these knowledge gaps, the present study implements 2D DNS of viscoelastic channel flow using the finitely extensible nonlinear elastic-Peterlin (FENE-P) model. Our

methodology adapts analytical frameworks originally developed for 3D DRT and EIT, enabling direct comparison with established 3D flow characteristics. Through this approach, we aim to: (1) establish comprehensive statistical descriptors for 2D EIT, (2) elucidate its unique dynamical processes, and (3) systematically contrast its features with 3D counterparts. The paper is structured as follows: Section 2 details the governing equations and numerical methodology, Section 3 presents comparative analyses of flow statistics and dynamical mechanisms, with concluding discussions provided in Section 4.

## 2. Numerical methodology

### 2.1. Governing equations

This study focuses on the 2D plane Poiseuille flow of incompressible viscoelastic fluid. The channel walls are considered to be non-slip, and the periodic boundary condition is imposed in the streamwise direction. The normalization is performed using the channel half-height  $h$ , the bulk average velocity  $u_b$ , the time  $h/u_b$ , and the pressure  $\rho u_b^2$  as characteristic scales of length, velocity, time and pressure. Here,  $u_b = \frac{1}{2h} \int_{-h}^h \bar{u}(y) dy$  with  $\bar{u}(y)$  the locally averaged velocity in the streamwise direction;  $\rho$  is the density of fluid. The dimensionless governing equations are as follows:

$$\nabla \cdot \mathbf{u} = 0, \quad (2.1)$$

$$\frac{\partial \mathbf{u}}{\partial t} + \mathbf{u} \cdot \nabla \mathbf{u} = -\nabla p + \frac{\beta}{Re} \nabla^2 \mathbf{u} + \nabla \cdot \boldsymbol{\tau}_p, \quad (2.2)$$

where  $\mathbf{u} = (u, v)$  is the velocity vector;  $p$  is the pressure;  $\boldsymbol{\tau}_p$  is the additional elastic stress tensor;  $\beta = \eta/\mu$  is the viscosity ratio with  $\mu$  the dynamic viscosity of solution and  $\eta$  the contribution of solvent to the viscosity;  $Re = \frac{\rho u_b h}{\eta}$  is the average Reynolds number.

The viscoelastic fluid is described by Peterlin (FENE-P) model, based on which  $\boldsymbol{\tau}_p$  is obtained by:

$$\boldsymbol{\tau}_p = \frac{1 - \beta}{Re Wi} [f(r^2) \mathbf{C} - \mathbf{I}], \quad (2.3)$$

$$\frac{\partial \mathbf{C}}{\partial t} + (\mathbf{u} \cdot \nabla) \mathbf{C} - \mathbf{C} \cdot (\nabla \mathbf{u}) - (\nabla \mathbf{u})^T \cdot \mathbf{C} = -\frac{f(r^2) \mathbf{C} - \mathbf{I}}{Wi}, \quad (2.4)$$

where  $\mathbf{C}$  is the conformation tensor indicating the local state of the polymer solution with  $\mathbf{C} = \langle \mathbf{q}\mathbf{q} \rangle$  and  $\mathbf{q}$  the end-to-end vector of a pair of polymer molecules;  $Wi = \frac{\lambda u_b}{h}$  is the Weissenberg number;  $\lambda$  is the relaxation time of viscoelastic fluid; the Peterlin function  $f(r^2)$  is defined as  $f(r^2) = \frac{L^2 - 2}{L^2 - r^2}$  with  $r^2$  the trace of  $\mathbf{C}$  and  $L$  the maximum extension length of the polymer chains.

### 2.2. Numerical schemes

The above equations are solved by an in-house DNS code based on the staggered-grid finite difference method. For the spatial discretization, the second-order central difference scheme is adopted for the convection, pressure, diffusion, and elastic stress terms of the momentum conservation equation. For the time marching, a fractional step method is employed, where the pressure term uses an implicit scheme and other terms adopts the second-order Adams–Bashforth scheme. A time-splitting method is adopted to solve the governing equations, briefly described as follows: (1) calculating the conformation tensor and the elastic stress field by Eqs. (2.3) and (2.4); (2) conducting a partial time marching of

the velocity field in Eq. (2.2) to obtain the first intermediate velocity field; (3) substituting the first intermediate velocity field into the continuity equation (2.1) to get the pressure Poisson equation, and solving it to obtain the second intermediate velocity field; (4) applying an appropriate mean pressure gradient to the second intermediate velocity field with the pressure term to maintain a constant flow rate.

A striking highlight in the numerical algorithm is that, the tensor-based interpolation method we proposed (Zhang et al. (2023)) is adopted to address the well-known high Weissenberg number problem (HWNP). This method can guarantee the invariants and symmetric positive definite property of the conformation tensor without adding any artificial diffusion, so as to achieve feasible and accurate numerical simulation of high and ultra-high  $Wi$  viscoelastic fluid flow. The key of the tensor-based interpolation method is to interpolate the eigenvalues and orientation of the conformation tensor field  $\mathbf{C}$  rather than its components. The brief application steps are as follows:

- (i) Decomposing a known conformation tensor field  $\mathbf{C}$  by  $\mathbf{C} = \mathbf{R}\mathbf{\Lambda}\mathbf{R}^T$  to obtain  $\mathbf{R}$  and  $\mathbf{\Lambda}$ ;
- (ii) Calculating the Eulerian angles and eigenvalues at the grid node  $i$  by (2.5) and (2.6),

$$\mathbf{\Lambda} = \begin{bmatrix} \Lambda_1 & 0 & 0 \\ 0 & \Lambda_2 & 0 \\ 0 & 0 & \Lambda_3 \end{bmatrix}, \quad (2.5)$$

$$\mathbf{R} = \begin{bmatrix} \cos \theta \cos \varphi & \sin \psi \sin \theta \cos \varphi - \cos \psi \sin \varphi & \cos \psi \sin \theta \cos \varphi + \sin \psi \sin \varphi \\ \cos \theta \sin \varphi & \sin \psi \sin \theta \sin \varphi + \cos \psi \cos \varphi & \cos \psi \sin \theta \sin \varphi - \sin \psi \cos \varphi \\ -\sin \theta & \sin \psi \cos \theta & \cos \psi \cos \theta \end{bmatrix}, \quad (2.6)$$

where  $\mathbf{R}$  and  $\mathbf{\Lambda}$  are the rotation and the diagonal matrix, respectively;  $\psi$ ,  $\theta$  and  $\varphi$  the Euler angles relative to the Cartesian coordinate system;  $\lambda_1$ ,  $\lambda_2$  and  $\lambda_3$  are the eigenvalues;

- (iii) Obtaining the Eulerian angles and eigenvalues at the grid interface  $i+1/2$  through various interpolation schemes, and calculating  $\mathbf{\Lambda}_{i+1/2}$  and  $\mathbf{R}_{i+1/2}$  at the grid interface by (2.5) and (2.6) to reconstruct the conformation tensor  $\mathbf{C}_{i+1/2}$ .

In addition, various curve interpolation schemes can be used to obtain the Euler angles and eigenvalues on the grid interface, and then the conformation tensor at the grid interface can be obtained. So the convection term in equation 2.5 adopts the Weighted Essentially Non-Oscillatory (WENO) scheme (Shu (1998)). The details can be found in Zhang et al. (2021a, 2023) and Zhang et al. (2024).

### 2.3. Numerical conditions

Our latest work (Zhang et al. (2024)) demonstrated that the size of the computational domain has a significant effect on the achieved flow state of viscoelastic fluid. And even the occurrence of the steady arrowhead regime (SAR) state with low resistance is related with the shorter channel length. Only the simulation with a sufficiently long channel length can guarantee a fully developed EIT at high  $Wi$ . Moreover, the desired computational domain length of the simulated case has a functional relationship with  $Wi$ . Therefore, we use the sufficiently long channel ( $L_x \times L_y = 20h \times 2h$ ) to conduct long-time numerical simulations and statistical analysis. The grid is set to be uniform in streamwise direction and non-uniform in wall-normal direction to ensure that there are more dense grids near the wall. The grid distribution along the wall-normal direction is as follows:

$$y_j = \frac{1}{a} \tanh\left(\frac{1}{2}\delta_j \ln\left(\frac{1+a}{1-a}\right)\right), \quad (2.7)$$

where  $y_j$  is the location of the  $j$ -th grid node,  $\delta_j = -1 + 2j/N_y$  with  $N_y$  the total number of grids along the wall-normal direction,  $a$  is the regulatory parameter for the grid inequality

---

$Wi$	$Re$	$L$	$\beta$	$C_{f,tur} \times 10^{-3}$	$C_{f,lam} \times 10^{-3}$	Flow state
2	2000	100	0.9	/	3.00	L
8.8	2000	100	0.9	/	2.98	L
9	2000	100	0.9	2.99	/	EIT
10	2000	100	0.9	3.27	/	EIT
20	2000	100	0.9	3.97	/	EIT
40	2000	100	0.9	4.45	/	EIT
60	2000	100	0.9	4.75	/	EIT
80	2000	100	0.9	4.96	/	EIT
100	2000	100	0.9	5.10	/	EIT
150	2000	100	0.9	5.36	/	EIT
200	2000	100	0.9	5.58	/	EIT

---

Table 1: Numerical conditions and some results. “L” denotes the laminar flow;  $C_{f,lam}$  represents the friction factor of viscoelastic laminar flow.

---

degree and set to be  $a = 0.95$ . After the detailed grid independence validation in our recent work (Zhang et al. (2024)), the grid resolution is set to  $N_x \times N_y = 1024 \times 304$  and the time step is  $5 \times 10^{-4} h/u_b$  or the smaller. Table 1 shows the numerical conditions and some results of DNSs in this study. All simulations use the parameters same as the setup in Zhang et al. (2024) fixing  $Re = 2000$ ,  $\beta = 0.9$  and  $L = 100$ . A wide range of  $Wi$  is covered from 2 to 200. Also, it is observed that the flow states of  $Wi > 8.8$  are EIT. The observation is consistent with the results of Shekar et al. (2020) under the same  $Re$ . Notably, the characteristic velocity scaling differs between studies: while Shekar et al. (2020) employs the Newtonian laminar centerline velocity ( $U_c$ ), our study uses the bulk flow velocity ( $U_b$ ). This scaling difference creates a systematic offset, where our  $Wi = 10$  case corresponds to  $Wi_c = 15$  in Shekar et al. (2020). Subsequent analysis focuses on the cases of  $Wi \geq 10$  which captures the developed EIT dynamics.

### 3. Results and analysis

#### 3.1. Statistical analysis

We begin by presenting key findings from our flow statistical analysis. Figure 1 illustrates the profiles of mean streamwise velocity normalized by the inner scale across various  $Wi$ . Previous investigations (Dubief et al. (2013); Zhang et al. (2021a,b); Wang et al. (2023)) have established that 3D flows exhibit a systematic upward shift in velocity profiles with enhanced elasticity, ultimately approaching the MDR asymptote (Virk et al. (1970),  $u^+ = 11.7 \ln y^+ - 17.0$ ) from the IT baseline ( $u^+ = 2.5 \ln y^+ + 5.5$ ). In stark contrast, our 2D flow results reveal an inverse behavior: velocity profiles progressively deviate downward from the laminar state with increasing  $Wi$ , ultimately converging to a distinct asymptotic regime ( $u^+ = 6 \ln y^+ + 1.5$ ) when  $Wi = 200$ . This counterintuitive trend aligns with recent friction factor observations (Zhu et al. (2021)), collectively suggesting fundamentally different underlying mechanisms between dimensional configurations. This dimensional dichotomy stems from contrasting dynamical frameworks. In 2D flows, turbulence generation is exclusively governed by elasto-inertial instability (Sid et al. (2018); Zhu et al. (2021)), resulting in pure EIT devoid of IT components. Enhanced elasticity amplify EIT intensity, driving the velocity profile’s steady transition from laminar to turbulent characteristics. Conversely, 3D systems exhibit dual-regime turbulence (Wang et al. (2023)), where EIT

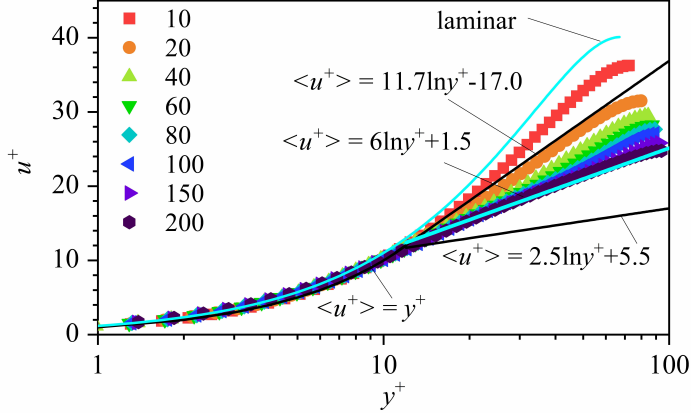


Figure 1: Mean velocity profiles normalized by the inner scale under different  $Wi$ .  $u^+$  and  $y^+$  are the dimensionless parameters normalized by the skin-friction velocity  $u_\tau = \sqrt{\tau_w/\rho}$  ( $\tau_w$  is wall shear stress) and the zero-shear-rate kinematic viscosity  $\nu = \mu/\rho$  of the solution.

and IT dynamics coexist in a competitive interplay. The dominance shift from IT to EIT with increasing  $Wi$  suppresses inertial contributions, ultimately steering the system toward MDR asymptotics. Notably, while 3D flows demonstrate progressive IT suppression and EIT ascendancy, 2D systems manifest unadulterated EIT intensification. This fundamental distinction inevitably produces divergent elastic responses in statistical flow descriptors. Regarding asymptotic behavior, neither the MDR nor IT asymptote appears to influence velocity convergence in 2D EIT systems. Furthermore, we hypothesize that the emergent asymptotic state may exhibit parametric sensitivity to variations in  $Re$ ,  $\beta$ , and  $L^2$ , suggesting potential avenues for future investigation.

Figure 2 shows the distributions of root mean square (rms) of the streamwise velocity  $u_{rms}$  and wall-normal velocity  $v_{rms}$  at different  $Wi$ . As is shown,  $u_{rms}$  and  $v_{rms}$  both tend to increase with  $Wi$  and eventually converge, which is similar to the trend observed in Figure 1 and opposite to those of the 3D flows (Wang et al. (2023)). This still reflects the different dynamical processes in 2D and 3D flows. For  $u_{rms}$ , the peak is increasingly larger, and gradually moves towards the channel wall with the increase of  $Wi$ . This indicates increasing velocity fluctuations near the wall and the existence of strong extension structures. For  $v_{rms}$ , the largest values are at the channel centre, which is consistent with that of 3D EIT with high  $Wi$  (Dubief et al. (2013); Wang et al. (2023)). In fact, for IT and DRT before the maximum drag reduction, the peak of  $v_{rms}$  profile appears far from the centre, which can be considered as a feature that distinguishes EIT from IT and non-MDR states. Moreover, the  $v_{rms}$  profile has apparently smaller value than the  $u_{rms}$  profile and nearly converges when  $Wi > 60$ , indicating the significant anisotropy of EIT.

In channel flow, the total flow drag can be composed of the Reynolds stress  $\tau_R$ , elastic stress  $\tau_e$ , and viscous stress  $\tau_v$ , governed by the stress balance equation:

$$\underbrace{-\overline{u'v'}}_{\tau_R} + \underbrace{\overline{\tau_{xy}}}_{\tau_e} + \underbrace{\frac{\beta}{Re} \frac{d\bar{u}}{dy}}_{\tau_v} = \tau_{total}, \quad (3.1)$$

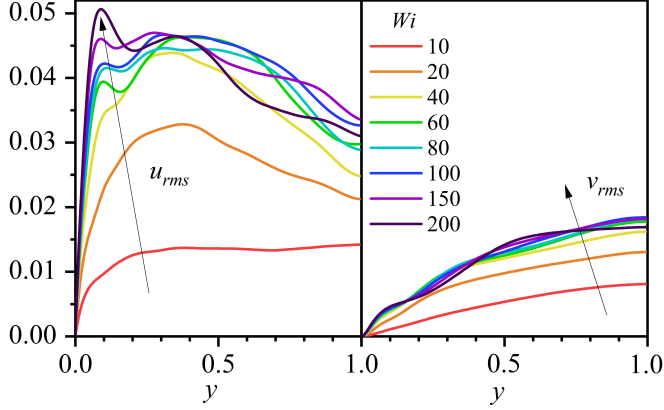


Figure 2: Distributions of r.m.s. of velocity fluctuations at different  $Wi$ .

where  $\overline{(\cdot)}$  represents the ensemble-averaged variable;  $(\cdot)'$  is the fluctuating variable and  $(\cdot)' = (\cdot) - \overline{(\cdot)}$ .

Figure 3 illustrates the distributions of mean  $\tau_v$ ,  $\tau_e$  and  $\tau_R$  at different  $Wi$ . Figure 3a reveals a non-monotonic trend in  $\tau_v$ , initially increasing before diminishing beyond a critical  $y$ -position, ultimately converging toward the channel center. Near the wall, enhanced elasticity amplifies the viscous stress contribution to flow resistance, though this effect becomes negligible near the channel center due to the rapidly decaying shear rate. Figure 3b demonstrates a monotonic increase in  $\tau_e$  with rising  $Wi$ , with peak magnitudes consistently localized between  $y = 0.2$  and  $y = 0.3$ . This behavior aligns with 3D flow observations (Wang et al. (2023)), reflecting the role of elasticity in intensifying EIT. However, contrary to the positive  $\tau_v$  and  $\tau_e$ , the  $\tau_R$  in Figure 3c consistently exhibits negative value although significantly lower than the other stresses. Its value grows with  $Wi$ , eventually approaching convergence. This finding deviates fundamentally from experimental measurements (Warholic et al. (1999); Samanta et al. (2013)) and 3D simulations (Dubief et al. (2013); Wang et al. (2023)), where Reynolds stress remains positive -albeit minimal- in the MDR state. The anomalous negative  $\tau_R$  further distinguishes 2D EIT from IT where Reynolds stress dominantly governs total drag. Detailed mechanistic insights into this phenomenon will be discussed in Section 3.2.

Figure 4 compares the distributions of mean polymer extension and the maximum relative polymer extension at different  $Wi$ . Specifically, as shown in Figure 4a, the extension levels within the central range are consistently lower than those of near-wall range, due to the smaller shear rate away from the wall. However, the extension saturation range has been obviously closer to the centre as  $Wi$  increases. In the absence of the suppression by Newtonian turbulence, the polymer extension in 2D EIT can easily reach a high degree as compared to 3D numerical simulations (Dubief et al. (2013)). At the same time, compared with the polymer extension in laminar flow ( $Wi = 2$ ), the local peak of turbulent profile away from the wall can be observed, which indicates the existence of the extensional flow topologies described by Dubief et al. (2013). In Figure 4b, by comparing with the maximum mean polymer extension of laminar flow at corresponding  $Wi$ , it is observed that EIT can provide an additional amount of extension. The additional extension is randomly distributed in the turbulent extension field (see Figure 7), manifesting as the characteristic polymer extension sheet structures of EIT. Moreover, the promoting effect of increasing elasticity on extension exhibits a saturation trend, which is precisely the embodiment of the effective elasticity

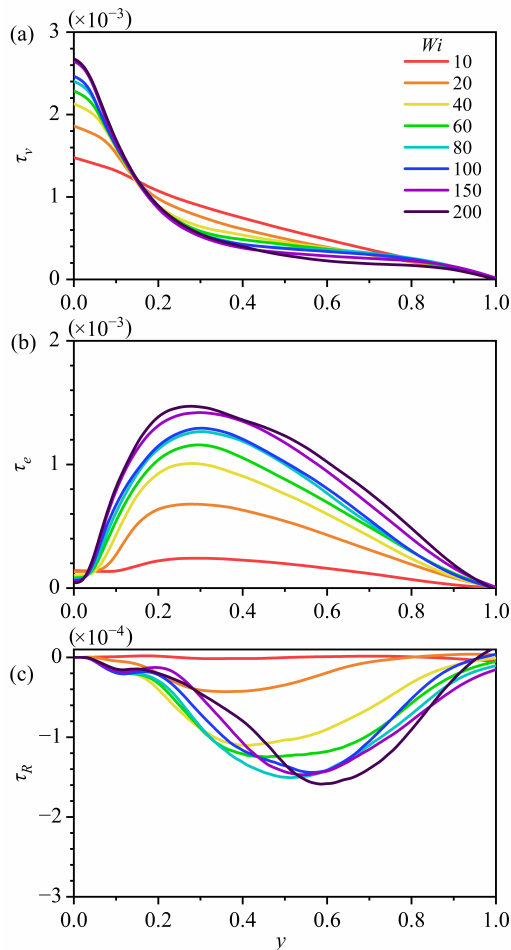


Figure 3: Distributions of three kinds of stress at different  $Wi$ .

(Zhang et al. (2024)) we have previously reported. At  $Wi=200$ , the maximum mean polymer extension reaches approximately 90%, and will continue to approach slowly 100% at ultra-high  $Wi$  (e.g.,  $Wi = 1000$ , not shown).

### 3.2. Anomalous Reynolds stress

The anomalous Reynolds stress behavior in EIT, as evidenced by Figure 3c, reveals fundamentally distinct momentum transport mechanisms compared to Newtonian turbulence. The quadrant analysis (Lu et al. (1973)) is frequently employed to study the Reynolds stress  $\tau_R$ . Through quadrant analysis, we systematically deconstruct this phenomenon by resolving the Reynolds stress  $\tau_R$  into four components based on the sign of velocity fluctuations  $u'$  and  $v'$ : Q1 (outward high-speed fluid motion), Q2 (low-speed fluid ejection), Q3 (inward low-speed motion), and Q4 (high-speed sweep motion). In IT, the classical dominance of Q2/Q4 motions drives substantial Reynolds stress production through intense bursting events (Lu et al. (1973)). For DRT of viscoelastic fluid, Cai et al. (2009) experimentally found that the existence of CTAC additives in viscoelastic fluid can suppress turbulent bursting motions, namely the ejection and sweep motions of Q2 and Q4. This led to drag reduction or rather the extremely small Reynolds stress. Similarly, in PAM solution flows, Guan et al. (2013)

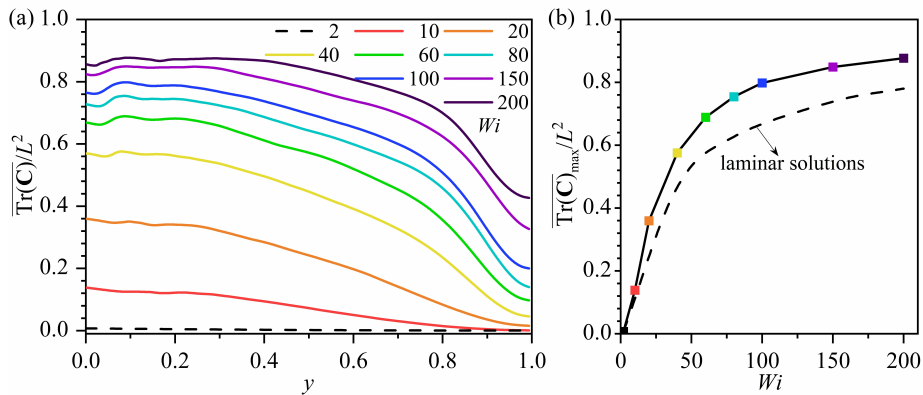


Figure 4: (a) Distributions of mean polymer extension  $\overline{\text{Tr}(\mathbf{C})}/L^2$  (the  $Wi = 2$  case is laminar flow), and (b) the maximum mean polymer extension at different  $Wi$  (the dashed line represents the maximum mean polymer extension of corresponding laminar solutions).

reported that the occurrence of small Reynolds stress is due to the significant decrease of ejections and sweeps of Q2 and Q4 near the wall. Figure 5 reveals two key evolutionary trends with increasing  $Wi$  including Q2/Q4 suppression and Q1/Q3 enhancement. The characteristic bursting motions diminish progressively, showing significant reduction in integrated stress contribution. In contrast, symmetric inward/outward motions intensify, generating a mid-channel stress peak ( $y \approx 0.4-0.6$ ) that dominates the anomalous stress profile. The inversion of quadrant dominance at high  $Wi$  directly explains the observed negative Reynolds stress. This phenomenon originates from elasticity-driven flow restructuring: polymer stresses amplify symmetric Q1/Q3 motions while suppressing asymmetric bursting events. Crucially, this dual effect persists across both 2D and 3D flow configurations, suggesting a universal EIT mechanism that fundamentally reorganizes turbulent momentum transport pathways. The self-sustaining nature of this regime likely stems from positive feedback between elastic stress accumulation and quadrant motion redistribution Zhang et al. (2024).

In order to clearly show the distribution characteristics of four quadrant components, Figure 6 presents the relevant probability density distributions in four quadrants at different positions. It is observed that for each  $Wi$  case, the distributions of probability density near  $(u', v') = (0, 0)$  are the most concentrated, which is the reflection of extremely small Reynolds stress value. Moreover, as the distance from the channel wall increases, the outline of distribution region gradually changes from an elongated strip to an irregular ellipse, indicating that the probability density begins to spread outward (towards the high-value region), especially for  $v'$ . The distribution characteristics are highly similar to the findings in 3D flow experiments (Guan et al. (2013)). However, the increasing probability of appearing in high-value region does not necessarily imply a corresponding increase of anomalous Reynolds stress at every point in the flow, due to the mutual restraint and offset among the four quadrants. For example, at  $y = 0.2$ , the small Reynolds stress is obviously due to the fact that  $v'$  has the significantly low-value level. Different from the situation at  $y = 0.2$ , at the channel center of  $y = 1.0$ , the probability distributions of high-value region in Q1 and Q4 are quite large. Figure 5 shows that at  $y = 1.0$ , the values in the upper and lower quadrants almost offset each other, resulting in zero Reynolds stress here. Nonetheless, at  $y = 0.4$  and  $y = 0.6$ , there is a noticeable presence of relatively larger Reynolds stress. As shown by the black dashed frames and arrows, the outlines of distribution regions are obliquely distributed along the first

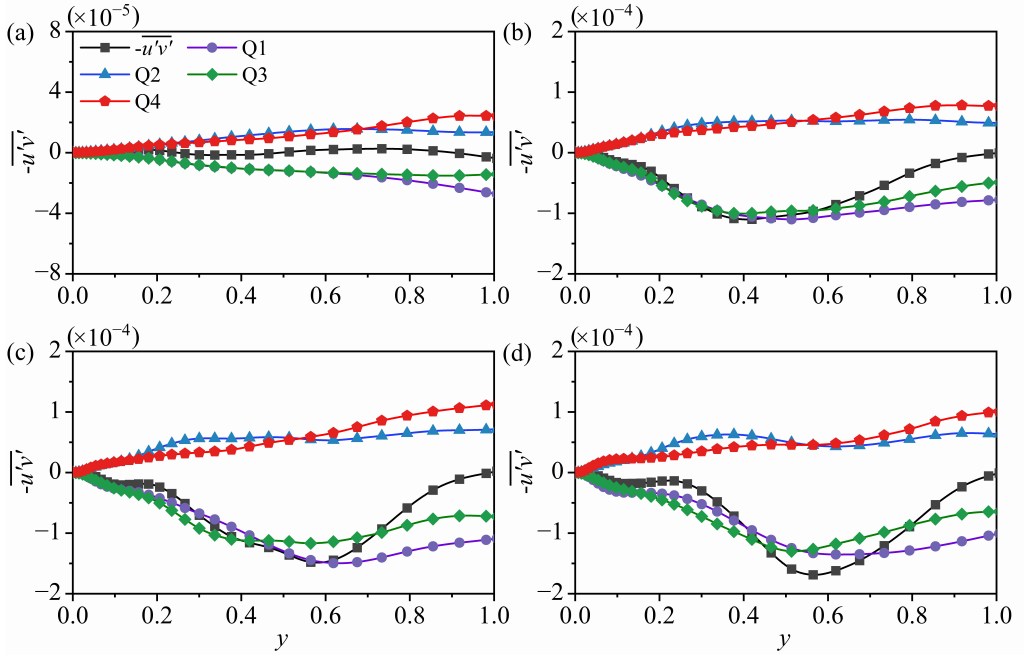


Figure 5: Quadrant distributions of Reynolds stress at different  $Wi$ : (a)  $Wi = 10$ ; (b)  $Wi = 40$ ; (c)  $Wi = 100$ ; (d)  $Wi = 200$ .

and third quadrants, which is in stark contrast to the diagonal distribution along the second and fourth quadrants in IT (Guan et al. (2013)). This indicates that the distributions in Q1 and Q3 are at high probability and high value levels, suppressing the positive contribution of Q2 and Q4 to Reynolds stress, which well explains the location of the peaks of Reynolds stress profiles in Figure 5. Therefore, contrary to the dominance of ejection and sweep motions in IT, the above demonstrates the significant dominance of the motions of Q1 and Q3 in 2D EIT.

Instead of focusing on the frequency and amplitude of the fluctuating velocity at the single position, a more comprehensive understanding can be obtained by analyzing the whole flow field. Figure 7 depicts the superposition of instantaneous polymer extension and fluctuating velocity vector field at  $Wi = 10, 40, 100$ , and  $200$ . These flow fields are all filled with many vortexes composed of fluctuating velocity vectors, each of which contains the fluctuating velocity vectors of four different quadrant components. The regions with concentrated Q1 and Q3 motions are highlighted by white and purple arrows, respectively. Combined with Figure 6, we can observe that Q1 and Q3 motions are dominant, and this situation becomes more significant as  $Wi$  increases. Take the black ellipse region in Figure 7b as an example, which can be approximately regarded as a large vortex. Clearly, the upper and lower parts within this region are undergoing two opposing processes of stretching and contraction of the polymer extension sheet-like structures. In the flow of viscoelastic fluid, the dynamic behavior of polymer chains is intricately linked to the velocity field. At a macro level, the stretching and contraction processes of the polymer extension sheet-like structures must be directly and closely related to the direction of fluctuating velocity vectors. Thus, a clear judgment can be obtained: the vast majority of fluctuating velocity vectors in the first and third quadrants, namely the motions of Q1 and Q3 are arranged along and against the polymer extension sheet-like structures, respectively. For the viscoelastic fluid flow, a

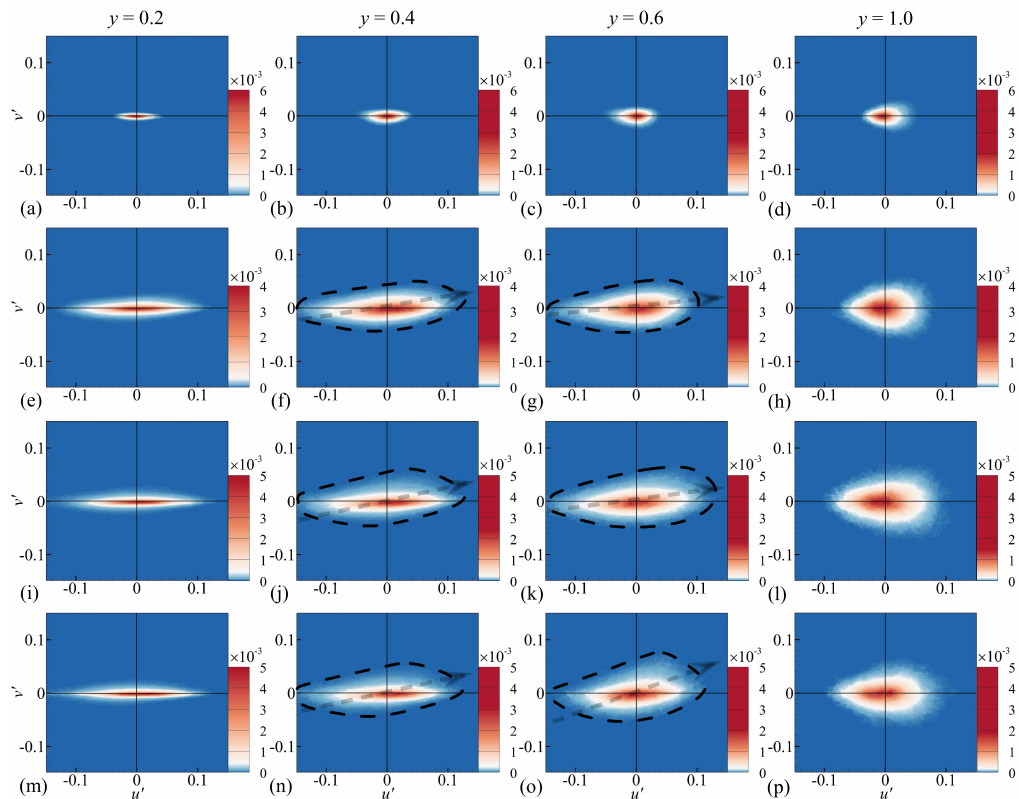


Figure 6: Probability density distribution contours of four quadrant components at different positions away from the wall (from left to right,  $y = 0.2, 0.4, 0.6,$  and  $1.0$ ): (a)-(d)  $Wi = 10$ ; (e)-(h)  $Wi = 40$ ; (i)-(l)  $Wi = 100$ ; (m)-(p)  $Wi = 200$  (the black dashed frames are used to show the outlines of distribution regions, with the black arrows meaning the oblique distributions).

typical characteristic is the presence of numerous elongated polymer extension sheet-like structures in the flow field, which exhibit the inclined distribution from the near-wall region towards the channel centre along the streamwise direction. This distribution becomes more pronounced as  $Wi$  increases, accompanied by the intensification of the anisotropy of the EIT. Thus, this distribution indicates that the fluctuating velocity vectors accompanying the polymer extension sheet-like structures are preferentially in the first or third quadrant. In 2D EIT, unencumbered by IT, this situation is even more pronounced, leading to anomalous Reynolds stress. Finally, comparing the results of 2D EIT with numerical (Dubief et al. (2013); Wang et al. (2023)) and experimental results (Samanta et al. (2013); Choueiri et al. (2018)) of 3D turbulent flow, it is evident that the Reynolds stress values in both cases are significantly lower than other stresses. However, it is noteworthy that although they are small enough to be negligible, the Reynolds stress in 3D flow is not negative. We speculate that the presence of residual other dynamics within the MDR state may be a contributing factor, which supports the view that the MDR state is not the pure EIT (Zhu et al. (2021)). Nevertheless, the existence of anomalous Reynolds stress indicates that EIT has a strong suppression on IT in the MDR state, and the degree of this suppression can be quantitatively measured by the variation of Reynolds stress.

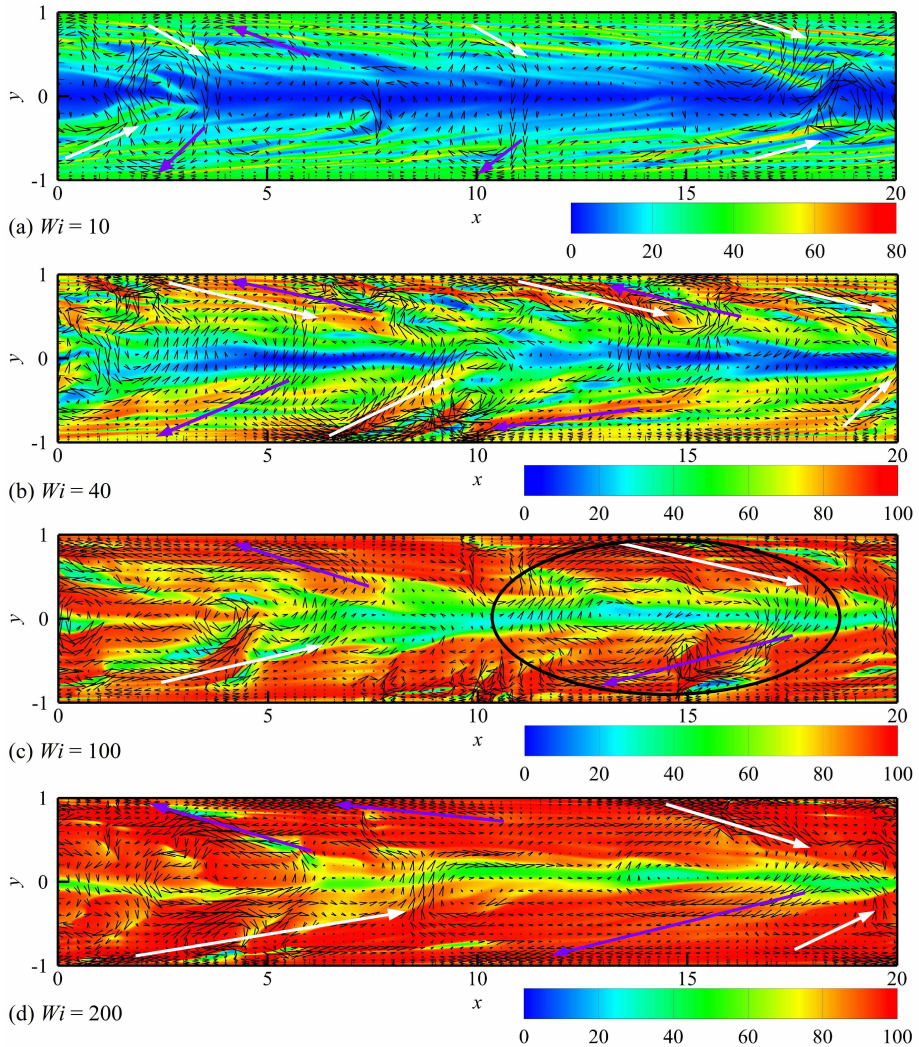


Figure 7: Superposition of the instantaneous extension and the fluctuating velocity vector field at  $Wi = 10, 40, 100,$  and  $200$  (the  $x$  direction is compressed by half for improved display).

### 3.3. Budgets of turbulent kinetic energy and elastic energy

In the MDR state, the negligible Reynolds stress cannot dominate the production of turbulent kinetic energy (TKE), and polymers provide almost all the energy required for turbulence maintenance (Min et al. (2003); Dubief et al. (2013); Wang et al. (2023)). Similarly, in the above section, the discovery of minimal and anomalous Reynolds stress also proves that the main source of TKE in EIT cannot possibly be the production term related to the Reynolds stress. Therefore, the energetic properties in 2D EIT are well worth exploring and compared with those of 3D flow. The transformation between the turbulent elastic energy (TEE) and TKE greatly distinguishes the viscoelastic fluid flow from the Newtonian fluid flow. The integral form of the budget of TKE is as follows:

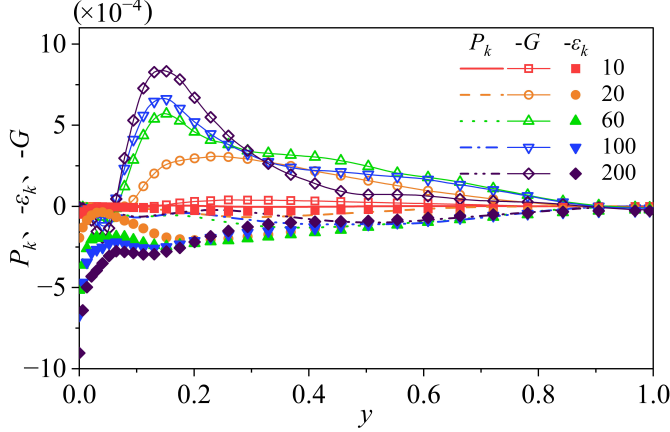


Figure 8: Profiles of turbulent kinetic energy budget at different  $Wi$ .

$$\int_0^2 P_k dy - \int_0^2 \varepsilon_k dy - \int_0^2 G dy = 0, \quad (3.2)$$

$$P_k = -\frac{1}{2} \overline{u'v'} \frac{\partial \bar{u}}{\partial y}, \quad \varepsilon_k = \frac{\beta}{\text{Re}} \overline{\frac{\partial u'_i}{\partial x_j} \frac{\partial u'_i}{\partial x_j}}, \quad G = \overline{\tau'_{ij} \frac{\partial u'_i}{\partial x_j}}, \quad (3.3)$$

where  $P_k$  is the production term of TKE,  $\varepsilon_k$  is the dissipation term, and  $G$  is the energy transfer term between TKE and TEE (the positive value of  $G$  indicates the transfer from TKE to TEE, while the negative value signifies the reverse process).

Similarly, the budget of TEE can be obtained by integrating the elastic energy transport equation:

$$\int_0^2 P_e dy - \int_0^2 \varepsilon_e dy + \int_0^2 G dy = 0, \quad (3.4)$$

$$P_e = \overline{\tau_e \frac{\partial \bar{u}}{\partial y}}, \quad \varepsilon_e = \frac{f(\text{tr}(\mathbf{C})) \tau_{ii}}{2Wi}, \quad (3.5)$$

where  $P_e$  is the production term dominated by elastic stress of TEE and  $\varepsilon_e$  is the dissipation term.

Figure 8 illustrates the profiles of the budget of TKE under varying  $Wi$ . In all cases, the primary source of TKE is consistently the energy transfer term  $-G$ : TEE is converted into TKE through the interaction between polymers and turbulent flow. Also, this feature is independent of  $Wi$ . However, this situation in which the generation of TKE is overwhelmingly dominated by  $-G$ , only occurs in the asymptotic MDR state or EIT of 3D flow at high  $Wi$  (Dubief et al. (2013); Wang et al. (2023)). Therefore, we can infer that EIT likely has already formed in actual 3D flow, but its partial features are obscured due to the coexistence with IT. Moreover,  $-G$  is reversed within a narrow region near the wall and this phenomenon also exists in 3D flow (Dubief et al. (2013); Wang et al. (2023)). The only difference lies in the fact that the production term  $P_k$  exhibits a negative value in 2D EIT, which is attributable to the aforementioned abnormal Reynolds stress. Nonetheless,  $P_k$  constitutes a small proportion in the budget of TKE, exerting a negligible impact on the self-sustaining mechanism of 2D EIT.

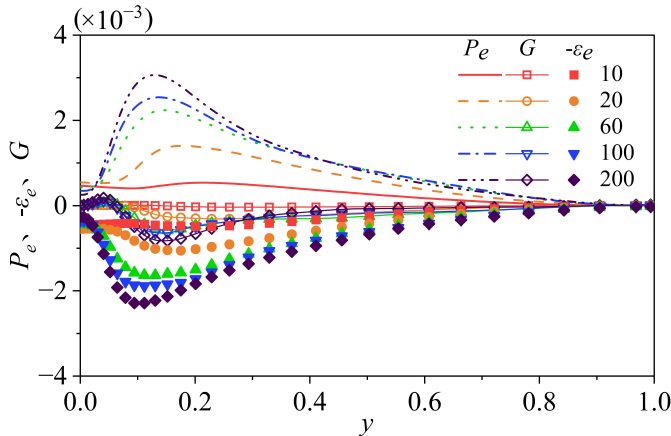


Figure 9: Profiles of elastic energy budget at different  $Wi$ .

Similar to Figure 8, Figure 9 shows the profiles of the budget of TEE at different  $Wi$ . The trend of each curve is consistent with the 3D simulation results (Zhang et al. (2021b)). The generation and dissipation of TEE are mainly concentrated in the near-wall region, resembling the distribution of the budget of TKE. However, unlike the generation of TKE derived mainly from  $-G$ ,  $P_e$  provides the vast majority of the generation of TEE, indicating the dominant role of the work done by the elastic stress. As  $Wi$  increases, the enhancement of the turbulent intensity of EIT is primarily driven by the increase of  $-G$ , yet there is a saturation trend. This is attributed to the concurrent increase of the dominant dissipation term  $\varepsilon_e$ , resulting in only a smaller fraction of TEE being converted into TKE. The unique TEE characteristics of EIT show remarkable consistency in the budget analysis of between 2D and 3D flow, which is also a strong evidence of the 2D nature of EIT.

### 3.4. Redistributive role of pressure

The above content provides a detailed analysis of the TKE budget of EIT. In fact, the majority of studies including this paper choose to use the pressure-driven flow, where the pressure play a critical role in the redistribution of energy among the components of momentum (Terrapon et al. (2015)). Moving forward, this paper will decompose the pressure into several parts and assess their roles in redistributing TKE.

Many scholars have analyzed the redistributive role of pressure in 3D turbulent flow of viscoelastic fluid (Ptasinski et al. (2003); Terrapon et al. (2015); Zhang et al. (2022)). As shown in equations (3.6-3.12), the pressure fluctuations can be decomposed into four contributing terms. As reported by Kim et al. (1989) and Terrapon et al. (2015), the rapid part  $p'_r$  is a direct and linear response to the change and deformation in the mean flow field, while the slow part  $p'_s$  is the response through nonlinear turbulent interactions. The distinctive polymer contribution  $p'_p$  exists in the viscoelastic flow due to the polymer stress. Notably, the first two terms ( $p'_r$  and  $p'_s$ ) and  $p'_p$  are identified as the inertial and elastic contributions, respectively (Terrapon et al. (2015); Zhang et al. (2022)). The inertia and nonlinear elasticity of the fluid play varying roles in the pressure redistribution effect and the self-sustaining process of EIT.

$$p'(\mathbf{x}) = p(\mathbf{x}) - \bar{p}(\mathbf{x}), \quad (3.6)$$

$$p'(\mathbf{x}) = p'_r(\mathbf{x}) + p'_s(\mathbf{x}) + p'_p(\mathbf{x}) + p'_{St}(\mathbf{x}), \quad (3.7)$$

$$\nabla^2 p'_r = -2 \frac{d\bar{u}}{dy} \frac{\partial v'}{\partial x}, \quad (3.8)$$

$$\nabla^2 p'_s = -\frac{\partial u'_i}{\partial x_j} \frac{\partial u'_j}{\partial x_i} + \frac{d^2 \overline{v'^2}}{dy^2}, \quad (3.9)$$

$$\nabla^2 p'_p = \frac{\partial^2 \tau'}{\partial x_i \partial x_j}, \quad (3.10)$$

$$\nabla^2 p'_{St} = 0, \quad (3.11)$$

$$\Phi_{ii} = 2p' \frac{\partial u'_i}{\partial x_i}. \quad (3.12)$$

where  $p'_r$ ,  $p'_s$ ,  $p'_p$ , and  $p'_{St}$  represent rapid, slow, polymer, and Stokes pressures, respectively; and the Stokes pressure  $p'_{St}$  reflects the role of the wall boundary condition, which is ignored due to its apparently small proportion;  $\mathbf{x} = (x, y)$ ,  $\otimes'$  represents fluctuations and  $\overline{\otimes}$  represents average quantities.

Figure 10 shows the r.m.s. distribution of various pressure contributions at different  $Wi$ . As is shown, these different kinds of profiles in 2D EIT are generally similar to the results of the MDR state (Terrapon et al. (2015)), characterized by smoothness but not complete flatness. However, in another research with the Oldroyd-B model (Zhang et al. (2022)), the r.m.s. profiles of 3D EIT exhibits a quasi-flat distribution. This difference likely arises from the effect of the maximum extension length  $L$  ( $L = \infty$  for the Oldroyd-B model,  $L = 100$  in this paper and  $L = 200$  in Terrapon et al. (2015)). Detailedly, with the increase of  $Wi$ ,  $p'_{rms}$  gradually increases and approaches convergence, which fits with the effective elasticity effect we proposed (Zhang et al. (2024)). Moreover, the  $p'_s$  r.m.s. values reflect that the contribution of slow pressure is distinctly smaller than the other contributions, in line with the findings by Terrapon et al. (2015) in 3D simulations: polymers have a strong suppression on the slow pressure contribution  $p'_s$ . However, for the contribution of rapid pressure  $p'_{rms}$ , there exists a decrease trend at high  $Wi$  ( $Wi > 80$ ), which is actually also slightly reflected in the slow pressure. Unlike the effect of relaminarization in the 3D flows with low  $Re$  (Zhang et al. (2022)), the reason here is the suppression effect of strong elasticity. Furthermore, Figure 11 illustrates the distribution of  $p'^s_{rms}/(p'^r_{rms} + p'^s_{rms})$  along the wall-normal direction. The increasing trend of this ratio indicates that the contribution of  $p'_s$  in the inertial pressure gradually approaches saturation. Consequently, the rapid pressure contribution  $p'_r$  is more significantly suppressed by polymers in 2D EIT. Notably, the visible bump or peak of  $p'_{rms}$  within  $y = 0.2-0.4$  in Figure 10a, unequivocally originates from the polymer pressure contribution  $p'_p$ , which is in stark contrast to the buffer layer of IT where the obvious peak in the pressure fluctuations stems from the slow pressure (Terrapon et al. (2015)). Therefore, especially at high  $Wi$ , the increase in total pressure is primarily attributed to the dominant modulating role of polymer pressure  $p'_p$  in the pressure redistribution effect.

According to Dubief et al. (2013), pressure plays a crucial role in redistributing energy, especially TKE, across the momentum components. Through a comprehensive analysis of Reynolds stress transport, Terrapon et al. (2015) decomposed the velocity-pressure gradient correlation term into pressure-strain and pressure-diffusion terms, and pointed out that the

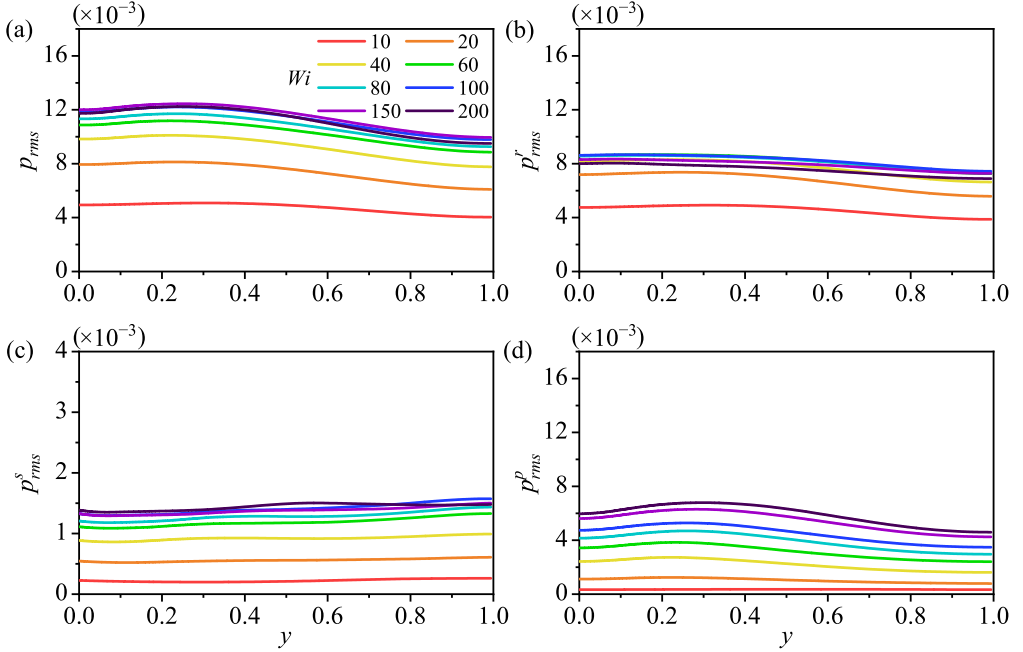


Figure 10: Pressure r.m.s. distribution along the wall-normal direction with different  $Wi$ : total (a), rapid (b), slow (c) and polymeric (d) contribution.

pressure-strain term  $\Phi_{ij}$  transports TKE from the streamwise direction to other directions. The trace of the pressure-strain term has an equality relation  $\text{tr}(\Phi_{ij}) = \Phi_{xx} + \Phi_{yy} + \Phi_{zz} = 0$  ( $\Phi_{zz}$  is not present in 2D simulations of this paper, and  $\Phi_{xx} = -\Phi_{yy}$ ). Figure 12 shows the distribution of the wall-normal pressure-strain component of total, rapid, slow and polymer pressure contributions at different  $Wi$  (streamwise pressure-strain component  $\Phi_{xx}$  is just the opposite, not shown). Overall, the distribution profiles of different pressure contributions show great consistency with the results of the MDR state as well as 3D EIT (Terrapon et al. (2015); Zhang et al. (2022)). Upon comparing the order of magnitude, we can intuitively discern the weak contribution of slow pressure in the energy transport of EIT in Figure 12c. However, unlike the inertial pressure, the polymer pressure contribution does not show an obvious convergence trend due to its elasticity nature, which is also the main source of the continuous enhanced TKE transport effect of pressure. And the  $\Phi_{yy}^p$  peak starts to be larger than the  $\Phi_{yy}^r$  peak at  $Wi > 40$ , which means that the polymer pressure dominates the TKE transport in 2D EIT.

As is shown in Figure 12, at approximately  $y < 0.1$ , all pressure contributions have negative wall-normal pressure-strain component, meaning that the TKE is redistributed from the  $y$  direction to  $x$  direction. Concurrently, in this range, the negative  $-G$  shown in Figure 8 indicates the conversion from TKE to TEE, thereby contributing to the characteristic turbulence streaks of viscoelastic flow (Zhang et al. (2022)). And the positive  $\Phi_{yy}$  at about  $0.1 < y < 0.4$  indicates the formation of wall-normal TKE within this range. Far from the wall (about  $0.5 < y < 1.0$ ), the formation of streamwise TKE occurs again, with the rapid pressure and polymer pressure dominating this process. In addition, near the channel center, the positive  $\Phi_{yy}^r$  and  $\Phi_{yy}^s$  indicates that the inertial pressure seems to have a promotion effect on the formation of wall-normal TKE, although offset by the negative effect of the polymer pressure. Notably, in fact, Terrapon et al. (2015) found that the polymer pressure

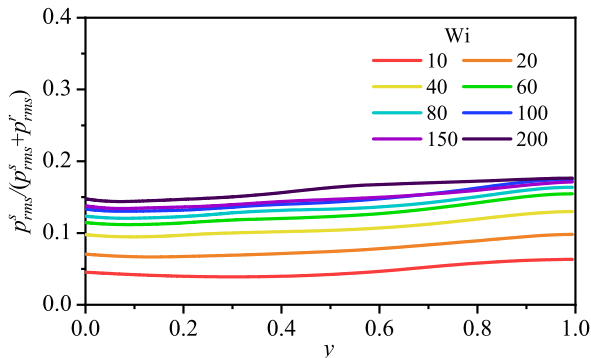


Figure 11: Distribution of the ratio of  $p_{rms}^S$  to  $(p_{rms}^R + p_{rms}^S)$  along the wall-normal direction.

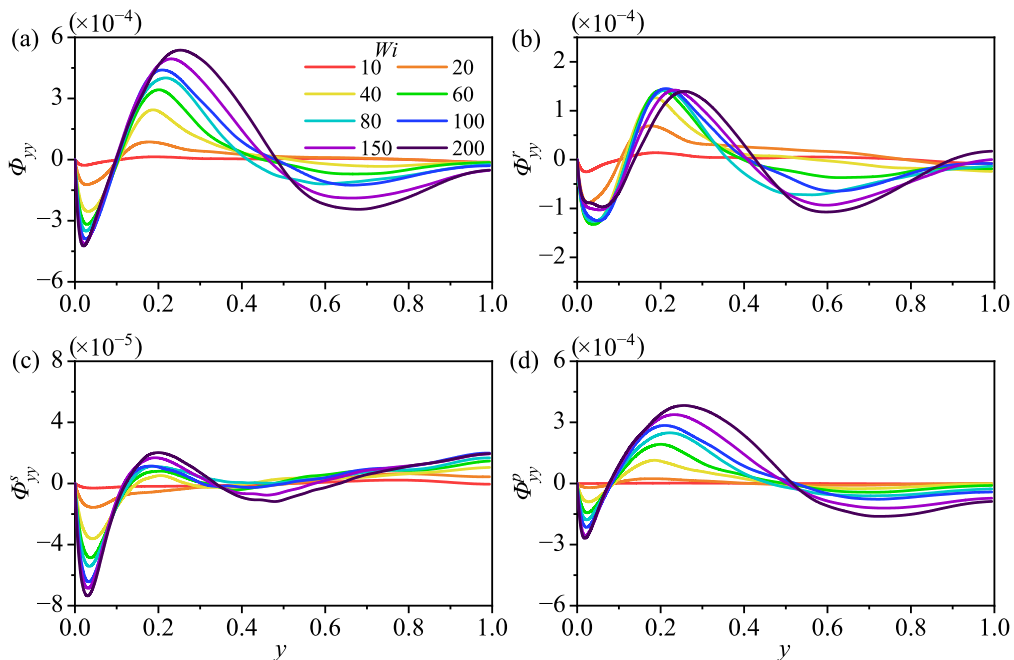


Figure 12: Distribution of wall-normal pressure-strain component  $\phi_{yy}$  from different pressure contributions under different  $Wi$ .

contributed more to  $\Phi_{yy}$  than  $\Phi_{zz}$ , in the analysis of 3D flow. They have argued that the elastic contribution promotes the 2D flow to a certain extent, while the inertial part mainly drives the 3D flow. Combined with the dominant role of polymer or elastic pressure on TKE transport of 2D EIT in Figure 12, it is again demonstrated that the 2D nature of elasto-inertial instability dominated by the elasticity in EIT and the objective existence of 2D EIT (Sid et al. (2018)).

### 3.5. Energy spectrum analysis

From the transformation between TEE and TKE in Figure 8 and Figure 9, it can be observed that the energy transformation occurs most intensely within the range of  $y = 0.1 \sim 0.2$ ,

which fully aligns with the characteristic position of energy transformation in 3D numerical simulations (Wang et al. (2023)). In order to delve deeper into the dynamics of 2D EIT, an energy spectrum analysis is conducted at this specific range, as well as at  $y = 0.4$  and the centreline of channel. Figure 13 shows the energy spectrum of TKE along the streamwise direction under different  $Wi$  at different wall-normal positions, with the corresponding power-law spectral decay  $k^{-\alpha}$  of interest. For these four different positions,  $\alpha$  shows a decreasing trend with  $Wi$ , and converges to a specific slope of the line at very high  $Wi$  (e.g.,  $Wi > 100$ ). In the near-wall energy spectrum of TKE in Figure 13a and b, the converging power-law decay of 2D EIT is  $k^{-11/3}$  within  $k > 10$ . Similarly, in 3D EIT, Dubief et al. (2013) found the power-law decay at high wavenumber seems to be closer to  $k^{-11/3}$  and deviate from  $k^{-14/3}$ , which is a support point for the 2D EIT. In the energy spectrum of  $y = 0.4$  in Figure 13c, it is observed that the  $k^{-19/6}$  power-law decay is present within a large range of  $k \approx 4 - 80$ , demonstrating the mighty presence of EIT dynamics in this region. However, for the 3D EIT, the  $k^{-19/6}$  power-law decay occurs due to the gradual conversion from  $-5/3$  power-law decay with the enhanced elasticity in the low wavenumber region (Zhang et al. (2021a)). Its appearance represents the prominent presence of EIT dynamics that gradually replaces IT dynamics. In the energy spectrum of the channel center in Figure 13d, there is also a special power law with  $-13/3$  at  $k \approx 5 - 60$ , which is between  $-11/3$  and  $-14/3$  and fits the power-law decay of 3D EIT (Dubief et al. (2013); Steinberg (2021)).

Fouxon et al. (2003) concluded that  $\alpha > 3$  through theoretical derivation, which is recognized as the theoretical power-law decay of ET (Steinberg (2021)). In contrast, the spectral properties of EIT have been poorly studied, but the  $k^{-\alpha}$  power-law decay with  $\alpha > 3$  for ET is also proved to be an available feature of EIT in experiments (Yamani et al. (2021)). Anyhow, all the above power-law decays for 2D as well as 3D EIT satisfy  $\alpha > 3$ . More strikingly, the trend of  $\alpha$  decreasing with  $Wi$  means that EIT is likely to have a close link to ET. In fact, under the same parameters, the  $\alpha$  for 3D flow exhibits a significant difference compared to that of 2D EIT (Sid et al. (2018)), which means that the convergence of power-law decay for 2D EIT requires higher  $Wi$ . It is more noteworthy that this also shows that the quantitative analysis of both 2D and 3D EIT is likely to encounter unsatisfactory situations, so the qualitative analysis is necessary. Therefore, to some extent, we can still find qualitatively the similarities between 2D and 3D EIT with high  $Wi$  in terms of the power-law decay, consistent with the viewpoint of Sid et al. (2018).

#### 4. Concluding remarks

Based on the DNSs of 2D sufficiently long channel flow of viscoelastic fluid, this paper qualitatively analyzes the statistical characteristics and underlying dynamic mechanisms of 2D EIT by compared with 3D flow.

(1) Firstly, the effects of elasticity on the statistical characteristics in 2D flow exhibit opposite trends compared with those of 3D flow. This is due to that, as  $Wi$  increases, IT is gradually suppressed in 3D flow, while EIT is gradually promoted in 2D flow. These two diverse processes of dynamic evolution inevitably mean opposite responses to elasticity variation.

(2) We have identified the anomalous Reynolds stress that contributes negatively to the flow resistance in 2D EIT. By quadrant analysis, it demonstrates that the motions in the first and third quadrants are dominant. And these motions are closely associated with the polymer sheet-like extension structures. Strikingly, they are inclined from the near-wall region towards the channel centre along the streamwise direction, which coincides with the distribution characteristics of the motions in the first and third quadrants. We believe that the

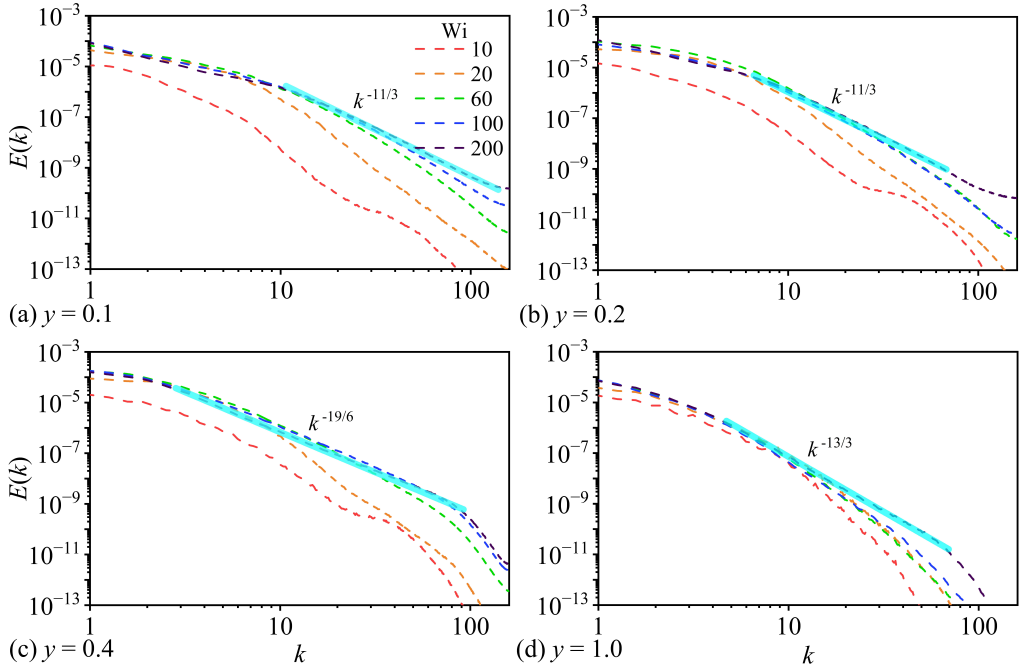


Figure 13: Energy spectrum at different  $Wi$  and wall-normal positions.

existence of anomalous Reynolds stress is inextricably linked to the formation of the typical structure of EIT.

(3) Finally, through the above analyses, such as the energy budget, redistributive role of pressure, energy spectrum characteristics and so on, we obtain the dynamic mechanisms of 2D EIT. In detail, TEE is almost entirely generated by elastic stress, which is then partly converted into TKE through the energy transfer term; subsequently, TKE is redistributed to different directions by the pressure, especially the critical and even dominant polymer pressure contribution, and The direction of redistribution differs in spatial location; lastly, over a wide high-wavenumber and small-scale range, the decay of TKE follows the unique power-law spectral decay  $k^{-\alpha}$  ( $\alpha > 3$ ) of viscoelastic turbulent flows. The sufficient similarities to those of 3D EIT convincingly confirms the objective existence of the 2D nature of EIT.

The exploration of 2D EIT still needs to be expanded and deepened. Similar to the study on altering  $Wi$  herein, the effects of other parameters such as  $Re$  and concentration also remain to be explored. Particularly, the link between EIT and ET under small  $Re$  will be highly anticipated. Looking further ahead, by conducting synchronized studies that encompass experiments as well as direct numerical simulations in both two and three dimensions, the future focus will be on unraveling the transition, in-depth mechanism and control of EIT.

## Acknowledgements

This research was funded by the National Natural Science Foundation of China (NSFC 52006249, 12202308, 12472255).

## Declaration of interests

The authors report no conflict of interest.

## REFERENCES

- BENEITEZ, M., PAGE, J., & KERSWELL, R. R. 2023 Polymer diffusive instability leading to elastic turbulence in plane Couette flow. *Phys. Rev. Fluids*, **8**, L101901.
- BENEITEZ, M., PAGE, J., DUBIEF, Y., & KERSWELL, R. R. 2024 Multistability of elasto-inertial 2D channel flow. *J. Fluid Mech.*, **981**, A30.
- BENEITEZ, M., PAGE, J., DUBIEF, Y., KERSWELL, R. R. 2024 Transition route to elastic and elasto-inertial turbulence in polymer channel flows. arXiv preprint [arXiv:2408.11508](https://arxiv.org/abs/2408.11508).
- BERTI, S., BISTAGNINO, A., BOFFETTA, G., CELANI, A., & MUSACCHIO, S. 2008 2D elastic turbulence. *Phys. Rev. E*, **77**(5), 055306.
- CAI, W. H., LI, F. C., ZHANG, H. N., LI, X. B., YU, B., WEI, J. J., KAWAGUCHI, Y., & HISHIDA, K. 2009 Study on the characteristics of turbulent drag-reducing channel flow by particle image velocimetry combining with proper orthogonal decomposition analysis. *Physics of Fluids*, **21**(11), 115103.
- CHAUDHARY, I., GARG, P., SHANKAR, V., & SUBRAMANIAN, G. 2019 Elasto-inertial wall mode instabilities in viscoelastic plane Poiseuille flow. *J. Fluid Mech.*, **881**, 119-163.
- CHOUERI, G. H., LOPEZ, J. M., & HOF, B. 2018 Exceeding the Asymptotic Limit of Polymer Drag Reduction. *Phys. Rev. Lett.*, **120**, 124501.
- CHOUERI, G.H., LOPEZ, J.M., VARSHNEY, A., SANKAR, S. & HOF, B. 2021 Experimental observation of the origin and structure of elastoinertial turbulence. *Proc. Natl Acad. Sci.* **118**(45), e2102350118.
- COUCHMAN, M. M. P., BENEITEZ, M., PAGE, J., & KERSWELL, R. R. 2024 Inertial enhancement of the polymer diffusive instability. *J. Fluid Mech.*, **981**, A2.
- DUBIEF, Y., WHITE, C., SHAQFEH, E. S. G., & TERRAPON, V. E. 2010 *Polymer Maximum Drag Reduction: A Unique Transitional State*. In *Annual Research Briefs*, pp. 395–404. Stanford, CA: Cent. Turbul. Res.
- DUBIEF, Y., & WHITE, C. 2011 Elastic turbulence in high Reynolds number polymer drag reduced flows. Abstract presented at APS Division of Fluid Dynamics Meeting, Baltimore, MD, Nov. 20–22, Abstr. M8–002.
- DUBIEF, Y., TERRAPON, V. E., & JULIO, S. 2013 On the mechanism of elasto-inertial turbulence. *Phys. Fluids*, **25**, 110817.
- DUBIEF, Y., PAGE, J., KERSWELL, R. R., TERRAPON, V.E., & STEINBERG, V. 2022 First coherent structure in elasto-inertial turbulence. *Phys. Rev. Fluids*, **7**, 073301.
- DUBIEF, Y., TERRAPON, V. E., & HOF, B. 2023 Elasto-inertial turbulence. *Annu. Rev. Fluid Mech.*, **55**, 675-705.
- FOUXON, A., & LEBEDEV, V. 2003 Spectra of turbulence in dilute polymer solutions. *Phys. Fluids*, **15**, 2060-2072.
- GARG, P., CHAUDHARY, I., KHALID, M., SHANKAR, V. & SUBRAMANIAN, G. 2018 Viscoelastic pipe flow is linearly unstable. *Phys. Rev. Lett.*, **121**, 024502.
- GILLISSEN, J. J. J. 2019 2D decaying elastoinertial turbulence. *Phys. Rev. Lett.*, **123**(14), 144502.
- GRAHAM, M. D. 2014 Drag reduction and the dynamics of turbulence in simple and complex fluids. *Phys. Fluids*, **26**(10).
- GROISMAN, A., & STEINBERG, V. 2000 Elastic turbulence in a polymer solution flow. *Nature*, **405**(6782), 53–55.
- GROISMAN, A., & STEINBERG, V. 2004 Elastic turbulence in curvilinear flows of polymer solutions. *New J. Phys.*, **6**(1), 29.
- GUAN, X. L., YAO, S. Y., & JIANG, N. 2013 A study on coherent structures and drag-reduction in the wall turbulence with polymer additives by TRPIV. *Acta Mech Sin.*, **29**, 485–493.
- HOF, B., SAMANTA, D., & WAGNER, C. 2011 The maximum drag reduction asymptote. Abstract presented at APS Division of Fluid Dynamics Meeting, Baltimore, MD, Nov. 20-22, Abstr. M8-005.
- KHALID, M., CHAUDHARY, I., GARG, P., SHANKAR, V. & SUBRAMANIAN, G. 2021 The centre-mode instability of viscoelastic plane Poiseuille flow. *J. Fluid Mech.* **915**, A43.
- LU, S. S., & WILLMARTH, W. W. 1973 Measurements of the structure of the Reynolds stress in a turbulent boundary layer. *J. Fluid Mech.*, **60**(3), 481–511.
- MIN, T., CHOI, H., & YOO, J. Y. 2003 Maximum drag reduction in a turbulent channel flow by polymer additives. *J. Fluid Mech.* **492**, 91-100.
- OSTWALD, W., & AUERBACH, R. 1926 Ueber die Viskosität kolloider Lösungen im Struktur-, Laminar- und Turbulenzgebiet. *Kolloid-Zeitschrift*, **38**, 261-280.
- PAGE, J., DUBIEF, Y., & KERSWELL, R. R. 2020 Exact travelling wave solutions in viscoelastic channel flow. *Phys. Rev. Lett.*, **125**, 154501.

- PTASINSKI, P. K., BOERSMA, B. J., NIEUWSTADT, F. T. M., HULSEN, M. A., VAN DEN BRULE, B. H. A. A., & HUNT, J. C. R. 2003 Turbulent Channel Flow near Maximum Drag Reduction: Simulations, Experiments and Mechanisms. *J. Fluid Mech*, **490**, 251-291.
- SAMANTA, D., DUBIEF, Y., HOLZNER, M., SCHAFER, C., MOROZOV, A. N., WAGNER, C., & HOF, B. 2013 Elasto-inertial turbulence. *Proc. Natl Acad. Sci.*, **110**, 10557.
- SHEKAR, A., MCMULLEN, R. M., WANG, S. N., MCKEON, B.J., & GRAHAM, M. D. 2019 Critical-layer structures and mechanisms in elasto-inertial turbulence. *Phys. Rev. Lett.*, **122**, 124503.
- SHEKAR, A., MCMULLEN, R., MCKEON, B. & GRAHAM, M. 2020 Self-sustained elasto-inertial Tollmien–Schlichting waves. *J. Fluid Mech*, **897**, A3.
- SHEKAR, A., MCMULLEN, R. M., MCKEON, B. J. & GRAHAM, M. D. 2021 Tollmien–Schlichting route to elasto-inertial turbulence in channel flow. *Rev. Fluids*, **6**, 093301.
- SHU, C. 1998 Essentially non-oscillatory and weighted essentially non-oscillatory schemes for hyperbolic conservation laws. Institute for Computer Applications in Science and Engineering.
- SID, S., TERRAPON V. E., & DUBIEF, Y. 2018 2D dynamics of elasto-inertial turbulence and its role in polymer drag reduction. *Phys. Rev. Fluids*, **3**, 011301.
- STEINBERG, V. 2021 Elastic turbulence: An experimental view on inertialess random flow. *Annu. Rev. Fluid Mech.*, **53**, 27-58.
- TERRAPON, V. E., DUBIEF, Y., & SORIA, J. 2021 On the role of pressure in elasto-inertial turbulence. *J. Turbul.*, **16**(1), 26-43.
- TOMS, B.A. 1949 Some observations on the flow of linear polymer solutions through straight tubes at large Reynolds numbers. Proc. 1st International Congress on Rheology, **2**, 135–141.
- VIRK, P.S., MICKLEY, H. S., & SMITH, K. A. 1970 The ultimate asymptote and mean flow structure in Toms' phenomenon. *Journal of Applied Mechanics*, **37**(2), 488-493.
- WANG, S.M., ZHANG, W.H., WANG, X.Y., LI, X.B., ZHANG, H.N., & LI, F.C. 2023 Maximum drag reduction state of viscoelastic turbulent channel flow: marginal inertial turbulence or elasto-inertial turbulence. *J. Fluid Mech*, **960**, A12.
- WANG, S. N., SHEKAR, A., & GRAHAM, M. D. 2017 Spatiotemporal dynamics of viscoelastic turbulence in transitional channel flow. *Journal of Non-Newtonian Fluid Mechanics*, **244**, 104-122.
- WARHOLIC, M. D., MASSAH, H., & HANRATTY, T. J. 2021 Influence of drag-reducing polymers on turbulence: effects of Reynolds number, concentration and mixing. *Experiments in Fluids*, **27**(5), 461-472.
- WARWARUK, L., & GHAEMI, S. 2024 Local flow topology of a polymer-laden turbulent boundary layer. *J. Fluid Mech*. **983**, A22.
- WHITE, C. M., & MUNGAL, M. G. 2008 Mechanics and prediction of turbulent drag reduction with polymer additives. *Annu. Rev. Fluid Mech.*, **40**, 235-256.
- XI, L., & GRAHAM, M. D. 2010a Turbulent drag reduction and multistage transitions in viscoelastic minimal flow units. *J. Fluid Mech*, **647**, 421-452.
- XI, L., & GRAHAM, M. D. 2010b Active and Hibernating Turbulence in Minimal Channel Flow of Newtonian and Polymeric Fluids. *Physical Review Letters*, **104**, 218301.
- XI, L., & BAI, X. 2016 Marginal turbulent state of viscoelastic fluids: A polymer drag reduction perspective. *Phys. Rev. E*, **93**, 043118.
- YAMANI, S., KESHAVARZ, B., RAJ, Y., ZAKI, T. A., MCKINLEY, G. H., & BISCHOFBERGER, I. 2021 Spectral Universality of Elasto-inertial Turbulence. *Physical Review Letters*, **127**, 074501 .
- YIN G., HUANG W. X., & XU C. X. 2018 Prediction of near-wall turbulence using minimal flow unit. *J. Fluid Mech.*, **841**, 654-673.
- ZHANG, W. H., ZHANG, H. N., LI, Y. K., YU, B., & LI, F. C. 2021a Role of elasto-inertial turbulence in viscoelastic drag-reducing turbulence. *Physics of Fluids*, **33**, 081706.
- ZHANG, W. H., SHAO, Q. Q., LI, Y. K., MA, Y., ZHANG, H. N., & LI, F. C. 2021b On the mechanisms of sheet-like extension structures formation and self-sustaining process in elasto-inertial turbulence. *Phys. Fluids*, **33**, 085107.
- ZHANG, W. H., ZHANG, H. N., WANG, Z. M., LI, Y. K., YU, B., & LI, F. C. 2022 Repicturing viscoelastic drag-reducing turbulence by introducing dynamics of elasto-inertial turbulence. *J. Fluid Mech*, **940**, A31.
- ZHANG, H. N., ZHANG, W. H., WANG X. Y., LI, Y. S., MA, Y., LI, X. B., & LI, F. C. 2023 On the role of tensor interpolation in solving high-WI viscoelastic fluid flow. *Phys. Fluids*, **35**, 031708.
- ZHANG, H. N., CHENG, H. T., WANG, S. M., ZHANG, W. H., LI, X. B., & LI, F. C. 2024 The minimal flow unit and origin of 2D elasto-inertial turbulence. *J. Fluid Mech*, **999**, A82.

ZHU, L., & XI, L. 2021 Nonasymptotic elastoinertial turbulence for asymptotic drag reduction. *Phys. Rev. Fluids*, **6**, 014601.